Impact of Carbon and Tungsten as Divertor Materials on the Scrape-off Layer Conditions in JET

M. Groth[1], S. Brezinsek[2], P. Belo[3], M.N.A. Beurskens[4], M. Brix[4], M. Clever[2], J.W. Coenen[2], C. Corrigan[4], T. Eich[5], J. Flanagan[4], C. Giroud[4], D. Harting[2], A. Huber[2], S. Jachmich[7], K.D. Lawson[4], M. Lehnen[2], C. Lowry[7], C.F. Maggi[5], S. Marsen[8], A.G. Meigs[4], G. Sergienko[2], B. Sieglin[5], C. Silva[3], A. Sirinelli[4], M.F. Stamp[4], G.J. van Rooij[9], S. Wiesen[2], and the JET-EFDA contributors[*]

JET-EFDA, Culham Science Centre, Abingdon, OX14 3DB, UK

[1]*Aalto University, Association EURATOM-Tekes, Espoo, Finland.*
[2]*Institute for Energy and Climate Research, Association EURATOM-FZJ Jülich, Germany.*
[3]*Institute of Plasmas and Nuclear Fusion, Association EURATOM-IST, Lisbon, Portugal.*
[4]*Culham Centre of Fusion Energy, EURATOM-Association, Abingdon, UK.*
[5]*Max-Planck Institute for Plasma Physics, EURATOM-Association, Garching, Germany.*
[6]*Association "EURATOM Belgium State", Lab. for Plasma Physics, Brussels, Belgium.*
[7]*EFDA Close Support Unit, Culham Science Centre, Abingdon, UK.*
[8]*Max-Planck-Institute for Plasma Physics, EURATOM Association, Greifswald, Germany.*
[9]*FOM Institute DIFFER, Association EURATOM-FOM, Nieuwegein, The Netherlands.*

e-mail contact of main author: mathias.groth@aalto.fi

Abstract. The impact of carbon and beryllium/tungsten as plasma-facing components on plasma radiation, divertor power and particle fluxes, and plasma and neutral conditions in the divertors has been assessed in JET both experimentally and by edge fluid code simulations for plasmas in low confinement mode. In high-recycling conditions the studies show a 30% reduction in total radiation in the scrape-off layer when replacing carbon (JET-C) with beryllium in the main chamber and tungsten in the divertor (JET-ILW). Correspondingly, at the low field side divertor plate a two-fold increase in power conducted to the plate and a two-fold increase in electron temperature at the strike point were measured. In low-recycling conditions the SOL was found to be nearly identical for both materials configurations. Saturation and rollover of the ion currents to both plates was measured to occur at 30% higher upstream densities and radiated power fraction in JET-ILW. Past saturation, it was possible to reduce the ion currents to the low field side targets by a factor of 2 and to continue operating in stable, detached conditions in JET-ILW; in JET-C the reduction was limited to 50%.

[*]*See the Appendix of F. Romanelli et al., Proceedings of the 24th IAEA Fusion Energy Conference 2012, San Diego, USA.*

These observations are in qualitative agreement with predictions from the fluid edge code package EDGE2D/EIRENE, for which a 30% reduction of the total radiated power is also yielded when switching from C to Be/W. For matching upstream parameters the magnitude of predicted radiation is, however, 50 to 100% lower then measured, independent of the materials configuration. Inclusion of deuterium molecules and molecular ions, and temperature and density dependent rates in EIRENE reproduced the experimentally observed rollover of the ion current to the low field side plate, via reducing the electron temperature at the plate.

1. Introduction

Radiation from impurities in the scrape-off layer (SOL) of tokamaks critically affects the SOL power balance and thus the power conducted to the divertor target plates. Carbon, in particular, strongly radiates in the temperature range characteristic of the divertor SOL (i.e., 10 to 50 eV), which is favourable for the reduction of power conducted to the divertor target plates. When changing the plasma facing components (PFCs) from all-carbon to metals in JET (JET-C and JET-ILW, respectively) in 2009/10 in one single shutdown [1], a significant loss of carbon radiation was anticipated, which in turn, was predicted to result in higher divertor heat loads. In addition, recycling of ions – in terms of the particle and energy reflection coefficients - is predicted to be higher off metallic surfaces than off a carbon surface [2], thus potentially leading to changes in the measurable divertor conditions for otherwise the same upstream plasma conditions. The present JET ITER-like wall consists of beryllium in the main chamber, including bulk Be in high heat flux areas, such as limiters, and Be-coated carbon-fibre composite (CFC) surfaces in the other, recessed areas. The divertor PFCs are made of bulk W for the horizontally inclined tiles at the low field side (LFS) and W-coated CFC surfaces in all the other divertor areas, including the vertically inclined targets at both the high field side (HFS) and LFS. Sets of reference plasmas in low-confinement mode (L-mode) with moderate auxiliary power of up to 3 MW were performed in both the JET-C and JET-ILW materials configurations to systematically characterise the

materials effect on the SOL conditions [3]. These plasmas included attached and detached plasmas in low and high triangularity magnetic configurations ($\delta \sim 0.2$ and 0.4, respectively) and the LFS strike point connected to the horizontal plate; the HFS strike point was always connected to the HFS vertical plate (Fig. 1). For simplicity, these configurations are herein named horizontal. To assess the divertor performance in ITER-relevant configurations, magnetic equilibria with both strike points on the vertical plates were also investigated. This report describes the analysis for the radiative losses in the SOL, the particle and heat fluxes to the divertor targets, and the plasmas conditions (electron temperature, T_e) at the divertor plates. The impact of the wall materials was also assessed numerically using the fluid edge code package EDGE2D/EIRENE [4]-[6], and its predictions of the primary SOL parameters are compared to the experimental data.

2. Comparison of attached L-mode plasmas in the JET-C and JET-ILW configurations

The SOL in attached (i.e., low and high recycling) divertor conditions was extensively characterised in both material configurations in low-power, neutral beam-heated L-mode plasmas; in the JET-ILW, the studies were extended toward detached plasmas. To facilitate EDGE2D/EIRENE simulations of these plasmas by maximising the radial extent of the computational grid, a low triangularity configuration ($\delta \sim 0.2$) with a large (magnetic) clearance to the top of the vessel was chosen (Fig. 1, black configuration). These experiments were conducted at machine parameters typical for JET in normal current and field direction ($\mathbf{B} \times \nabla B$ toward the divertor): plasma current, I_P, of 2.5 MA, toroidal field, B_T, on the magnetic axis of 2.5 T, resulting in an edge safety factor, q_{95}, of 3.4. The total input power, comprised of ohmic and neutral beam heating ranged from 2.8 to 3.0 MW, with neutral beam heating contributing 1.6 MW (Fig. 2a). The radiated power in the core, $P_{rad,core}$, increased approximately linearly with upstream density, n_{up}, from 400 kW at the n_{up} to 1.4 MW at the

n_{up}. Here, n_{up} refers to the line-averaged density at the edge of the core plasma (minimum normalised radius at 0.9). Different values for n_{up} were achieved by deuterium gas fuelling from the top and divertor regions. In these plasmas the tungsten concentration in the center of the plasma deduced from VUV spectroscopy [7] was of the order $5x10^{-6}$ at the lowest n_{up}, and decreased below $1x10^{-6}$ at intermediate and the highest n_{up}. Consequently, W radiation contributed only 10% to 20% to $P_{rad,core}$, hence $P_{rad,core}$ was dominated by bremsstrahlung and other high-Z impurities, such as Ni. Hence, approximately 2.6 MW was transported from the core into the SOL.

In both materials configurations, the total power radiated in the SOL, $P_{rad,SOL}$, increased linearly with n_{up}, and saturated for JET-ILW as the divertor legs started to detach (Fig. 2b). At low n_{up} the radiation is dominated by radiation from the divertor, whereas at higher n_{up} up to 50% of the radiation came from the main SOL and the divertor X-point region. Visible spectroscopy across the divertor legs indicated that deuterium and carbon in JET-C, and deuterium and, to a lesser degree, beryllium in JET-ILW are the main contributors toward $P_{rad,SOL}$. Radiation from tungsten in the SOL is negligible, in particular for intermediate and high n_{up}. Integration of the radiation over the divertor legs ($P_{rad,div}$) indicated that $P_{rad,div}$ saturated before the rollover of the ion currents in JET-C (Fig. 2b), and was about 30% higher than in the JET-ILW for high-recycling conditions. While for the same n_{up} in low-recycling conditions the 2-D profiles were dominated by radiation from the HFS divertor leg ($P_{rad,HFS\ Div}$), radiation from the LFS leg ($P_{rad,LFS\ Div}$) was measured to be twice as high in high-recycling conditions (Fig. 3). In the high-recycling conditions, $P_{rad,LFS\ Div}$ is about twice as high in JET-C than in JET-ILW. These observations are consistent with the reduction in the carbon content in JET-ILW measured by charge exchange and visible spectroscopy: a ten-fold decrease in the C^{6+} density at the LFS midplane and low charge state carbon emission in the LFS divertor were observed [8]. Similarly, by going from JET-C to JET-ILW the effective

charge state, Z_{eff}, was reduced from 1.6 to 1.4 at the lowest n_{up}, and from 1.4 to 1.1 at intermediate n_{up}.

Consequently, for low-recycling conditions the power conducted to the LFS plate ($P_{div,LFS}$) was nearly identical in the JET-C and JET-ILW configurations, whereas for high-recycling conditions, $P_{div,LFS}$ was about a factor of 2 lower in JET-C (Fig. 2d). For these plasmas the power to the HFS, $P_{div,HFS}$, was measured in JET-C only, and was about a factor of two lower than $P_{div,LFS}$. Thus, balancing the input power against the radiated and conducted power to the plates for JET-C, 85% of the input power can be accounted for with the remaining power either going to the main chamber wall or are within the uncertainties of the combined measurements.

Nearly identical (within 50%) ion currents to the HFS and LFS plates ($I_{div,HFS}$ and $I_{div,LFS}$, respectively) were measured in low and high recycling conditions in both JET-C and JET-ILW (Fig. 4a and 4b). In JET-ILW, both $I_{div,HFS}$ and $I_{div,LFS}$ continued to increase and saturated halfway through the scanned density range. The total ion currents were derived from spatially integrating underneath the profile of the measured ion saturation current (j_{sat}). To improve the spatial resolution of the Langmuir probe measurements for j_{sat}, T_e and the electron density (n_e), strike point sweep at constant fuelling for several seconds were applied; in addition fuelling ramps were performed to cover the entire density range within one single discharge. As shown in Figs. 4a and 4b, the resulting current measurements are almost identical, however, there are distinctly different at the rollover density: the data from the fuelling ramp show a sharp reduction of I_{div} at slightly lower n_{up} than those observed in steady-state plasmas. It is important to note that for JET-ILW the rollover of $I_{div,HFS}$ and $I_{div,LFS}$ occurred at the same n_{up} and at radiated power fraction of approximately 50%. In JET-ILW, the density limit was reached at 65% of the Greenwald density and a radiated power fraction of 65%.

In both JET-C and JET-ILW, the peak T_e is significantly lower at the HFS than at the LFS in low-recycling conditions (Fig. 4c and 4d). This observation is consistent with previous measurements in JET [9] and other tokamaks (e.g., [10], [11], [12]), and can be explained by **E**x**B** drifts in the private flux region. As n_{up} was increased, $T_{e,pk,LFS}$ dropped sharply from 25 eV to 8 eV at the rollover of $I_{div,LFS}$ (Fig. 4d). In the case of the JET-ILW data, $T_{e,pk,LFS}$ continued to decrease to 2 eV, and likely even further as the Langmuir probe analysis becomes affected by non-Maxwellian electrons [13]. For JET-C, $T_{e,pk,LFS}$ dropped to 8 eV at distinctly lower n_{up} than for JET-ILW: within the limited dataset, at about 20-30% lower n_{up}. Similarly, being the derived quantity of j_{sat} and T_e, the peak n_e at the LFS plate increased with n_{up}, rolled over at the same n_{up} when $I_{div,LFS}$ peaked, and then decreased to nearly zero when the LFS divertor leg becomes detached. The reduction of $n_{e,pk,LFS}$ beyond the rollover of $I_{div,LFS}$ is consistent with the ionisation front moving off the LFS plate and toward the X-point region, which was directly inferred for the same set of discharges from Stark broadening analysis using a spectrometer in the visible wavelength range [14]. Since $I_{div,LFS}$ is identical in high recycling conditions, and $T_{e,pk,LFS}$ lower in JET-ILW than in JET-C at the same n_{up}, $n_{e,pk,LFS}$ is consequently higher for intermediate densities in JET-ILW.

Interpretation of the Langmuir probe data is significantly more challenging on the HFS plate than on the LFS plate because of a gap between the two vertical plates (see Fig. 1). The peak T_e and n_e on the HFS plate given in Figs. 4c and 4e are therefore shown for completeness and discussion of general trends. For both JET-C and JET-ILW, the Langmuir probes gave $T_{e,pk,HFS}$ in the range of 5 to 15 eV for the lowest to intermediate densities, with little dependence on the target materials (Fig. 4c). For JET-ILW, at n_{up} of the rollover of $I_{div,LFS}$, $T_{e,pk,HFS}$ appears to increase slightly compared to $T_{e,pk,HFS}$ observed at lower n_{up}, before dropping to temperatures of 1-2 eV. However, the significance of the trend $T_{e,pk,HFS}$ is unclear at the writing of this report. The peak n_e at the HFS plate generally follows the trend in

$I_{div,HFS}$ and increased with nup, before rolling over and decreasing when the HFS divertor became detached: $n_{e,pk,HFS}$ was measured 3 to 5 times higher in JET-C than in JET-ILW (Fig. 4e).

The deuterium input, pumping, and the recycling in the LFS divertor was observed to be similar within a factor of two in these L-mode plasmas for both JET-C and JET-ILW (Fig. 5). Firstly, to reach the same n_{up}, slightly lower deuterium fuelling rates were required in JET-ILW in the intermediate density range; however, the trend in the fuelling rates is almost identical (Fig. 5a). Secondly, the molecular deuterium pressure in the subdivertor pumping plenum was observed virtually identical between JET-C and JET-ILW: with increasing n_{up}, $p_{sub\text{-}div}$ increased exponentially over two decades at nearly identical pressures. (The data at the highest n_{up} in JET-ILW are truncated because the pressure gauge went into saturation.) Thirdly, line emission from deuterium atoms and molecules in the visible wavelength range (deuterium Balmer-α) measured across the LFS divertor leg reflects the Langmuir probe and neutral pressure measurements: D_α emission increased exponentially with n_{up} and only saturated at the highest n_{up}. The data suggest that the D_α emission was observed to be consistently higher by about a factor of 2 to 3 in JET-C compared to JET-ILW (Fig. 5d); however, taken the uncertainties in the measurements in account, the D_α emission must be assumed the same. At the HFS, however, D_α emission was consistently higher, by almost two orders of magnitude at the lowest n_{up}, in JET-C indicating lower temperatures and higher densities in this material configuration. To some degree, this observation is consistent with the larger $n_{e,pk,HFS}$ as measured by the Langmuir probes in JET-C. Further validation of these inferences, including consistency checks with other optical diagnostics measuring L_β and D_α emission in the same poloidal regions are pending at the writing of this report.

3. Comparison of detached L-mode plasmas in the carbon and ILW configurations

Corresponding cases of detached L-mode plasmas for both JET-C and JET-ILW were obtained in neutral-beam heated, high upper triangularity ($\delta \sim 0.4$) configurations in horizontal divertor plasma configurations, similar to those described in section 2 (Fig. 1, red configuration). As close as possible matching machine parameters were chosen for JET-C and JET-ILW: I_P = [2.0 / 2.0] MA, B_T on axis = [3.1 / 2.9] T, $P_{ohm} + P_{NBI}$ = [3.9 / 3.5] MW. The resulting power across the separatrix was about 3.4 MW for JET-C wall and 3.1 MW for JET-ILW (Fig. 6a). These plasmas were continuously fuelled with deuterium from the divertor region keeping the magnetic configurations stationary including the strike point positions. Since this experiment was performed in a single discharge and executed only once, the extent and quality of the experimental data are significantly reduced compared to the low triangularity case described in section 2.

In both JET-C and JET-ILW $P_{rad,SOL}$ and $P_{rad,div}$ increased nearly linearly with n_{up}, and in JET-ILW saturated just below the density limit (Fig. 6a): $P_{rad,div}$ was consistently lower by up 50% in JET-ILW than in JET-C (Fig. 6b), which is qualitative agreement with the data obtained in the low triangularity plasmas. For both materials configurations the density limit occurred at a radiated power fraction of about 50% of the total input power, and at about 20% lower n_{up} for the JET-C, consistent with additional investigations into the density limits [15]. As observed for the low triangularity configurations the required deuterium input to reach the same n_{up} is the same for JET-C and JET-ILW (Fig. 6c).

The rollover of $I_{div,HFS}$ and $I_{div,LFS}$ into detachment occurred at 30% higher n_{up} in JET-ILW than in JET-C (Fig. 7a and 7b). At matched input power the difference in the rollover density between the two materials configurations are likely to be somewhat smaller; however, it can still be assumed distinctly higher in JET-ILW. A similar inference can be drawn from the molecular deuterium measurements in the subdivertor (Fig. 6d): reaching the same pressure

both materials configurations required approximately 20% higher n_{up} in the JET-ILW. Most notably, for both materials configurations the rollover of I_{div} at the HFS and LFS occurred at the same n_{up}. At the rollover density $P_{rad,SOL}$ was of the order 1.2 MW for both materials cases, corresponding to a radiated power fraction of 35% and 42% for JET-C and JET-ILW, respectively. This is somewhat lower than what was observed in the low-triangularity configuration in JET-ILW. Beyond rollover, I_{div} at the HFS decreased with increasing n_{up} by an order of magnitude for both materials configurations. At the LFS and for JET-ILW, $I_{div,LFS}$ steadily decreased with n_{up} and was reduced by a factor of 2 compared to its peak value at rollover. In comparison, in JET-C $I_{div,LFS}$ saturated when increasing n_{up} past rollover, and only decreased by 25% close to the density limit. The continuous increase in the degree of detachment with n_{up} in JET-ILW – constituting itself in 30% higher n_{up} past rollover – permitted operation of partially and fully detached divertor plasmas in a much more stable fashion in JET-ILW than in JET-C. Due to the lack of data in the low and intermediate recycling regime the actual degree of detachment, as defined by Loarte et al. [16], cannot be derived based on the present data.

For the same n_{up} in conditions when the divertor legs are fully detached, the strength of recycling as indicated by D_α measurements are similar within 50% across the HFS leg and factors of 2 to 3 higher across the LFS leg (Fig. 7c and 7d). The latter observation is qualitatively consistent with (about 5 times) higher $I_{div,LFS}$ measured for JET-ILW (Fig. 7b); however, the root cause for this behaviour is yet not understood. For both JET-C and JET-ILW D_α emission saturates at the highest n_{up} achieved. Measurements of P_{div}, $T_{e,LFS}$, and $n_{e,LFS}$ of the detail required for making a quantitative assessment do unfortunately not exist for these plasmas.

4. Comparison of divertor plasma configurations

The effect of the divertor plasma configuration on the divertor conditions was investigated in attached L-mode plasmas in both JET-C wall and JET-ILW, and in ohmically heated, attached and detached plasmas in JET-ILW. Two different divertor plasma configurations were considered: (a) those with the LFS strike point on the horizontal plate, and (b) those with the LFS strike point on the vertical plate (Fig. 1, black and blue configurations; also insert Fig. 8a). In both configurations, the HFS was on the vertical plate.

For the same upstream conditions, very similar divertor plasma parameters (I_{div}, T_e, and n_e) were measured for the two materials combinations and in the two divertor plasma configurations (Figs. 8c and 8d); however, the vertical configuration was significantly better pumped than the horizontal configuration (Fig. 8b). The ohmic plasmas presented in Fig. 8 were executed at same I_p (2.0 MA) and B_T (2.0 T), and thus had the same ohmic input power (1.2 MW at the lowest n_{up} to 2.0 MW at the highest n_{up}). These plasmas were fuelled with deuterium from the top and divertor regions, and the fuelling was continuously increased to raise the n_{up} up to the density limit, while keeping the magnetic shape, including the strike points stationary. The total radiated power was identical between the two configurations.

Approximately twice as much deuterium fuelling was necessary to reach the same n_{up} in the vertical configuration as in the horizontal configuration, driven by the higher deuterium pressure in the pumping plenum and thus higher particle throughput (Figs. 8a and 8b). Higher divertor neutral densities in the vertical configuration is further corroborated by D_α emission measurements across the divertor legs, whose magnitudes were up to an order of magnitude higher in the vertical configuration, in particular across the HFS leg (Figs. 8e and 8f).

Between the horizontal and vertical configurations, I_{div} rolled over at slightly (~10%) lower n_{up} in the vertical configuration. The total magnitude of the ion currents are uncertain within a factor of 2 due to the lack of dedicated strike point sweeps to map out the profile. The rollover

occurred at a SOL radiative power fraction of 40%, which is consistent with the L-mode cases. A nearly symmetric dependence of I_{div} at the HFS and LFS plates on n_{up} was observed, in particular for the vertical configuration: both $I_{div,HFS}$ and $I_{div,LFS}$ peaked at the same n_{up} (Fig. 8c and 8d). Stable, partially detached divertor conditions were obtained for n_{up} nearly twice the value at rollover. Finally, the density limit was observed to be 30% higher in the vertical configuration.

5. EDGE2D/EIRENE predictions of the measured radiation profiles and divertor conditions

Utilising the measured profiles of electron density and temperature obtained at the LFS midplane, the 2-D multi-fluid edge code EDGE2D [4] coupled to the neutral Monte Carlo code EIRENE [5],[6] was used to predict the radiation profiles and divertor parameters as obtained experimentally. Here, emphasis is given to the low-triangularity, horizontal configuration, which has the most extensive experimental database to validate the simulations [17]. Simulations of the high-triangularity case can be found in ref. [18]. The two material configurations were adapted as they were, including Be in main chamber and W in the divertor for JET-ILW. The code package was substantially upgraded to include impurity sputtering due to other impurities and revised sputtering yields [19]. Migration of Be from the main chamber into the divertor, and deposition and subsequent re-erosion on the W surfaces were not modelled, i.e., pristine W surfaces in the divertor were assumed. While this may be an appropriate assumption for the LFS plate, Be-rich surface layers are expected along the HFS plate. W transport was modelled with a six-charge state bundling scheme. Carbon as a third impurity species in the Be/W simulations was yet not invoked, which is to some degree justifiable by the low carbon content observed experimentally. A thorough validation of these assumptions, including cross-comparison of predicted to measured emission from neutral and

low charge state Be and C ions, will be presented in future publications utilising the same setup of the simulations. Cross-field drifts (**E**x**B** and **B**x∇B) are not included in these simulations; hence, the analysis focuses on the LFS divertor only. The simulations were executed on two sets of grids: (a) one common grid corresponding to the JET-ILW magnetic configuration to assess the predictions for JET-C and JET-ILW on an otherwise identical setup, and (b) two separate grids corresponding to the magnetic configurations of the actual pulses to compare to the experimental data. A diffusive radial transport model with radially varying coefficients (shown in Figs. 9a and 9b) was applied to approximate the measured upstream profiles of n_e, T_e, and T_i for the lowest density case (Figs. 9c and 9d). The same model was then also applied for all the other (higher) densities forcing the simulations to match n_e at the separatrix, and to both the C and Be/W simulations (Figs. 9e-f). The conditions for the total power crossing the grid core boundary were derived from the power balance in the core, varying between 2.2 MW for the lowest n_{up} and 2.8 MW for the highest n_{up}. In doing so, the upstream T_e profiles were matched for all n_{up}; however, a penalty is paid by underestimating the pedestal and core n_e for n_{up} higher than the lowest n_{up}. Hence, particle confinement must improve (lower D_{perp}) with increasing n_{up}.

Fully converged solutions were obtained at densities corresponding to the experimental values of n_e at the separatrix at the LFS midplane ($n_{e,sep,LFS\text{-}mp}$). In addition, in raising the fuelling rate continuously from a low rate (matching the lowest density in the experiments) up to rates corresponding to the simulated density limit produces sets of quasi steady-state solutions. Both techniques produced the same functional dependencies of divertor parameters on $n_{e,sep,LFS\text{-}mp}$. The fuelling and pump locations were adapted as in the experiments: deuterium molecules were injected either at the top (JET-C) or divertor (JET-ILW), and removed in the corners of the divertor. Interchanging the fuelling locations had an insignificant effect on the divertor parameters: injecting deuterium in the divertor lead to 5% lower ion currents to the

HFS and LFS plates. EDGE2D/EIRENE was run with its standard, linearised version of the coupling scheme [6], but to simulate detached plasmas, a more complete EIRENE model was also employed, which includes both elastic and inelastic collisions between deuterons and deuterium molecules, collisional-radiative rates describing reactions between electrons and deuterium molecules, and reactions involving deuterium radicals (D_2^+) [20]. The inclusion of these reactions produced stable solutions predicting the peak T_e at the LFS plate to drop from of 0.9 eV to 0.3 eV (Fig. 10f), and thereby dropping both $I_{div,LFS}$ by 40% (Fig. 10e). The extension of the EIRENE model also leads to up to 10% higher P_{rad}, most predominately observed for JET-ILW and in $P_{rad,Be}$ radiation; hence, the combination of higher $P_{rad,tot}$ and lower $T_{e,pk,LFS}$ resulted in factor of 2 lower $P_{div,LFS}$. Because of the lower plasma temperature in the divertor when running with the extended compared to the linearised EIRENE model, the neutral fluxes into the divertor corners (mimicking the pumping ducts) are predicted 3 to 4 times higher. For attached plasmas both EIRENE models provided identical solutions (with the exception of $P_{div,LFS}$ for JET-ILW, which root cause is not understood).

Switching the wall materials from C to Be/W while keeping all other parameters in the simulations the same leads to an approximate 40% reduction of the total radiated power in the SOL (Fig. 10a). To isolate the switch of the wall materials, the simulations shown in Fig. 10 were executed on exactly the same grid, with the same boundary conditions (e.g., power across the core boundary, deuterium injection and pumping, etc.), and radial transport model. The simulations predict that the reduction in $P_{rad,tot}$ is driven by replacing C radiation with (mainly) Be radiation ($P_{rad,C} \approx 4 \times P_{rad,Be}$, Fig. 10c), while deuterium radiation is predicted virtually identical (Fig. 10b). Tungsten radiation only plays a role at $T_{e,pk,LFS} > 100$ eV. Correspondingly, the simulations for JET-ILW predict, for low-recycling conditions, 20% higher $P_{div,LFS}$ (Fig. 10d) than their JET-C comparison cases. Both $P_{div,LFS}$ and $T_{e,pk,LFS}$ are consistently predicted to be higher in the JET-ILW cases, and reach 200 kW and 2 eV at

about 10% higher $n_{e,sep,LFS\text{-}mp}$ in the JET-ILW than in the JET-C cases. Similarly, the predicted $I_{div,LFS}$ does not significantly change magnitude, but rolls over at about 10% lower $n_{e,sep,LFS\text{-}mp}$ for JET-ILW (Fig. 10e). There is no significant difference in the neutral fluxes into the divertor pumping plenum when switching wall materials, hence the neutral pressures near the pump may also be assumed the same.

Adapting the actual (experimental) equilibria of the plasmas in JET-C and JET-ILW, including the wall materials, and the location of deuterium injection and pumping, EDGE2D/EIRENE underestimates the measured $P_{rad,tot}$ in the SOL and pedestal region by about 50 % (Fig. 11a and 11b). For JET-C the discrepancy is even more pronounced when considering the radiation in the divertor only ($P_{rad,tot,div}$, Fig. 11c). While experimentally $P_{rad,tot,div}$ increased with $n_{e,sep,LFS\text{-}mp}$, and only saturated at the n_{up}, the simulations indicate a reduction of divertor radiation when the divertor plasma is detached. (In the simulations the loss in $P_{rad,tot,div}$ is compensated by an increase in radiation in the main SOL.) Despite the apparent lack of predicted radiation to match the measurements, the predictions also underestimate the $P_{div,LFS}$ for low-recycling conditions in both JET-C and JET-ILW, and for high-recycling and detached conditions in the JET-ILW case (Fig. 11e and 11f). The remaining power is predicted to be mostly conducted to the HFS target, overestimating the measured $P_{div,HFS}$, and a small fraction to the main chamber wall. Increasing the power crossing the grid core boundary – which is supported by the experimental data for higher core densities, thus higher ohmic heating – did not lead to a significant increase in $P_{rad,tot}$. Doing so, however, it moved $P_{div,LFS}$ closer to the measurements. Experimental uncertainties, for example, in the bolometer tomographic reconstructions and spatial integration of the profiles, and measuring very low power fluxes with an infrared camera may explain the observed discrepancies between the measurements and simulations. Inclusion of the cross-field drift

terms has also shown to produce higher $P_{rad,SOL}$ in the HFS leg, thus lower $P_{div,HFS}$, and higher $P_{div,LFS}$ [21] for the same n_{up}.

As shown for the generic comparison of predictions for JET-C and JET-ILW, inclusion of a more comprehensive neutral model in EIRENE was key to achieving rollover of $I_{div,LFS}$ and numerically stable, detached divertor plasmas in the simulations (Fig. 11g and 11h, also ref. [18] for the high triangularity cases). Without the model extension, $I_{div,LFS}$ would saturate at a certain (maximum) level, but not decrease significantly. Quantitatively, the predictions are within a factor of 2 of the measurements. Simultaneously, introducing the extended EIRENE model also increased the momentum losses by a factor of 2 when the plasma is detached. Raising the power across the grid core boundary had the effect of increasing the magnitude of $I_{div,LFS}$ and shifting the predicted rollover toward higher upstream densities.

With increasing upstream density the predicted peak electron temperature at the LFS plate fell from 70 to 100 eV to 0.5 eV at the rollover of $I_{div,LFS}$ (Fig. 11i and 11j). Further increase of $n_{e,sep,LFS\text{-}mp}$ dropped $T_{e,peak,LFS}$ further toward 0.3 eV. As for $I_{div,LFS}$, raising the upstream power shifted the required upstream density for dropping below 1 eV to higher values, and thereby moved the predictions away from the experimental data. The predicted D_α line emission integrated across the LFS divertor leg increases with $n_{e,sep,LFS\text{-}mp}$ and is generally within a factor of 2 to 3 within the measurements (Fig. 11k and 11l). The predictions show that the leg-integrated D_α saturates at the onset of $I_{div,LFS}$ rollover - which is much more pronounced for the predictions of the JET-C cases – and then increases again when the divertor plasma temperatures drop below 2 eV. Hence, D_α follows the trend of the particle fluxes (I_{div}) for the high-recycling regime, and T_e for the detached regime, as expected.

For the same $n_{e,sep,LFS\text{-}mp}$ and power across the core grid boundary, the simulations predict significantly (up to an order of magnitude) lower $T_{e,sep,LFS}$ for the vertical divertor plasma configuration compared to the horizontal configuration (Fig. 12). The simulations also show a

stronger rate of reduction of $T_{e,sep,LFS}$ with $n_{e,sep,LFS-mp}$ for the vertical configuration, and rollover of $I_{div,LFS}$ at 20% lower $n_{e,sep,LFS-mp}$. These results are driven by preferential emission of neutrals from the plates toward the separatrix in the vertical configuration and are consistent with those shown in ref. [22] and therein. The predictions are in qualitative agreement with the measurements obtained in ohmic plasmas (Fig. 4), but are more pronounced in the simulations than observed experimentally. The simulations were carried out for the JET-ILW materials configuration, but qualitatively do not differ from predictions for JET-C.

5. Summary

For a set of JET ohmic and L-mode plasmas in high-recycling conditions, replacing the carbon (JET-C) wall with a Be/W (JET-ILW) wall in JET reduced the radiated power in the divertor by 30%, and correspondingly increased the power conducted to the plate and electron temperature by up to a factor of 2. The reduction in radiated power is consistent with the measured, approximately ten times lower carbon content in the plasma in the JET-ILW. In low-recycling conditions the SOL plasmas are nearly identical between the two materials configurations. The rollover of the divertor ion currents as well as the density limit occurred at approximately 30% higher upstream density in the JET-ILW. Stable detached divertor plasmas with a significantly larger operational window in upstream density space were obtained in JET-ILW: beyond partial detachment, $I_{div,LFS}$ steadily decreased with upstream density and was reduced by a factor of 2 compared to its peak value at rollover; in JET-C a 25% reduction of $I_{div,LFS}$ only was obtained. Rather remarkably, for these magnetic configurations the rollover of $I_{div,HFS}$ and $I_{div,LFS}$ occurred at the same upstream densities for both materials configurations. Within a factor-of-two similar deuterium Balmer-α emission in the LFS divertor plasmas and subdivertor pressures indicate that the neutral behaviour in the

LFS divertor did not significantly differ between the two materials configurations. On the other hand, an order of magnitude lower D_α emission across the HFS divertor leg in JET-ILW would suggest that the HFS divertor is generally hotter in the JET-ILW configuration compared to JET-C; this could not conclusively be shown by Langmuir probe measurements on the HFS plate. Electron temperatures of the order 5 eV were obtained at upstream densities distinctly lower (~30%) than those at rollover of $I_{div,LFS}$; they are reduced further to 1 eV, and likely below, when the LFS divertor plasma was fully detached. Generally, the total deuterium input to reach the same upstream density is similar in JET-C and JET-ILW within a factor of 2.

Studies of horizontal and vertical configurations in ohmic plasmas indicate that latter configurations are better pumped. An order of magnitude increase in the D_α emission across the HFS divertor leg, and factor of 2 increase of D_α across the LFS divertor leg were observed in the vertical configuration compared to the horizontal one; the subdivertor pressure is also higher by a factor of 2 in the vertical configuration. Hence, to reach the same upstream density the deuterium input had to be increased by factors of 2 to 3.

For otherwise identical setups, simulations with the edge code package EDGE2D/EIRENE predict a 30% reduction of the radiated power in the SOL, which is consistent with the measurements. For both wall materials the simulations show the rollover of the divertor ion current at intermediate densities and steady decrease when increasing the upstream density beyond that: the rollover is less pronounced in JET-C as observed experimentally. Key to obtaining these results is the inclusion of additional reaction rates relating to deuterium molecules, molecular ions, and temperature and density dependent rate coefficients in EIRENE. The reduction of the divertor currents is driven by the decrease of the electron temperatures at the plate, which decrease from 0.9 eV to 0.3 eV when extending EIRENE. However, the simulations underestimate the radiated power in the SOL, and in particular the

radiated power in the divertor, independent of the materials configuration. The predicted power conducted to the LFS plate is, however, within the uncertainties and limitations of the measurements. We expect that inclusion of cross-field drifts, which is presently implemented in EDGE2D/EIRENE, will raise the power to the LFS plate, and decrease it to the HFS plate, and thus making it more consistent with the experimental data. For a corresponding vertical configuration and the same upstream conditions as in a horizontal configuration, the simulations predict up to an order of magnitude lower electron temperature at the separatrix on the LFS plate, as observed in previous calculations (ref. [22] and therein). Further validation of the simulations against spectroscopic measurements in the divertor is necessary to determine the dominant radiator and the plasma composition; these studies are presently carried out and will be presented in future publications.

Acknowledgment

This work was supported by EURATOM and carried out within the framework of the European Fusion Development Agreement (EFDA). The views and opinions expressed herein do not necessarily reflect those of the European Commission.

References

[1] MATTHEWS, G.F. et al., Phys. Scr. **2011** (2011) 014001.

[2] ECKSTEIN, W., Suppl. Nucl. Fusion **1** (1991) 17.

[3] BREZINSEK, S., et al., J. Nucl. Mater. **415** (2011) S936.

[4] SIMONINI, R., et al., Contrib. Plasma Phys. **34** (1994) 368.

[5] REITER, D., et al., J. Nucl. Mater. **196–198** (1992) 80.

[6] WIESEN, S., JET ITC-Report, http://www.eirene.de/e2deir_report_30jun06.pdf (2006).

[7] PUETTERICH, T., et al., Plasma Phys. Control. Fusion **50** (2008) 085016.

[8] BREZINSEK, S., et al., accepted J. Nucl. Materials, December 2012.

[9] CHANKIN, A.V., et al., Plasma Phys. Control. Fusion **36** (1994) 1853.

[10] HILL, D.N., et al., J. Nucl. Mater. **176-177 (**1990**)** 158.

[11] HUTCHINSON, I.H., et al., Plasma Phys. Control. Fusion **37** (1995) 1389.

[12] WISCHMEIER, M., et al., J. Nucl. Mater. **S415** (2011) 523.

[13] BATISHEV, O.V., et al., Phys. Plasmas **4** (1997) 1672.

[14] MEIGS, A.G., et al., submitted to J. Nucl. Materials, August 2012.

[15] HUBER, A., et al., submitted to J. Nucl. Materials, August 2012.

[16] LOARTE, A., et al., Nucl. Fusion **38** (1998) 331.

[17] GROTH, M., et al., accepted J. Nucl. Materials, December 2012.

[18] GUILLEMAUT, C., et al., submitted to J. Nucl. Materials, August 2012.

[19] HARTING, D., et al., submitted to J. Nucl. Materials, August 2012.

[20] KOTOV, V., et al., Plasma Phys. Control. Fusion **50** (2008) 105012.

[21] COSTER, D.P., et al., *Proc. 32nd EPS Conf. on Plasma Physics* (2012) P1.008.

[22] LOARTE, A., Plasma Phys. Control. Fusion **43** (2001) R183.

[23] BOBOC, A., et al., Rev. Sci. Instrum. **81** (2010) 10D538.

[24] BEURKENS, M.N., et al., Nucl. Fusion **48** (2008) 095004.

[25] BRIX, M., et al., Rev. Sci. Instrum. **83** (2012) 10D533.

[26] SILVA, C., et al., submitted to J. Nucl. Materials, August 2012.

[27] EICH, T., et al., J. Nucl. Mater. **415** (2011) S856.

[28] MONK, R.D., et al., J. Nucl. Mater. **241-243** (1997) 396.

[29] KRUEZI, U., et al., Rev. Sci. Instrum. **83** (2012) 10D728.

[30] HUBER, A., et al., Fus. Eng. Design **82** (2007) 1327

[31] MORGAN, P.D., et al., Rev. Sci. Instrum. **56** (1985) 862.

Figure captions

Fig. 1: Magnetic equilibria (separatrix only) of low triangularity (black, blue) and high triangularity configurations (red), and horizontal (black, red) and vertical (blue) divertor plasma configurations. The principal diagnostics used in these studies are highlighted: an inferometer with a line of sight across the SOL and pedestal regions at LFS midplane [23], a high-resolution Thomson scattering (HRTS) system [24], a lithium beam system [25], a reciprocating probe [26], a vertical viewing infrared thermography (HFS and LFS plates for JET-C, LFS plate for JET-ILW only) [27], an array of target Langmuir probes [28], and a baratron/Penning pressure gauge system [29]. The total radiated power was measured with a multiple-chord bolometer system and reconstructed tomographically [30], and the Balmer-α emission with two vertical viewing systems integrating over the HFS and LFS divertor regions [31]. The two latter systems are not shown.

Fig. 2: Total input power and radiated power in the core (a), radiated power in the entire SOL and in the divertor (b), total radiated power in the HFS and LFS divertor legs (c), and total conducted power to the HFS and LFS plates (d) as function of line-averaged edge density. Black symbols refer to JET-C, the red symbols to JET-ILW.

Fig. 3: 2-D tomographic reconstruction of the total radiated power as measured by bolometry for low recycling ($<n_e>_{l,edge}$ = 1.1 x 10^{19} m^{-3}) conditions (a,b) and high-recycling ($<n_e>_{l,edge}$ = 2.4 x 10^{19} m^{-3}) conditions (c,d). The data pertaining to JET-C are in the left-hand column (a,c) and to JET-ILW in the right-hand column (b,d).

Fig. 4: Total ion currents to the HFS (a) and LFS plates (b), and the peak electron temperatures (cod) and densities (e,f) at the HFS and LFS plates as function of line-averaged edge density. Colours as in Fig. 2.

Fig. 5: Total deuterium atom input (a), molecular deuterium pressure in the subdivertor near the cryo pump (b), and divertor leg integrated D_α brightness across the HFS (c) and LFS legs (d) as function of line-averaged upstream density. Colours as in Fig. 2.

Fig. 6: Total power across the separatrix and total radiated power in the main chamber and divertor SOL (a), total radiated power in the divertor region (b), total deuterium atom input (c), and molecular deuterium pressure in the subdivertor. The data pertain to the high triangularity plasmas; black symbols refer to JET-C, and the red symbols to JET-ILW.

Fig. 7: Total ion currents to the HFS (a) and LFS (b) plates, and divertor leg integrated D_α brightness across the HFS (c) and LFS legs (d) as function of line-averaged upstream density. Colours as in Fig. 6.

Fig. 8: Total deuterium atom input (a), molecular deuterium pressure in the subdivertor (b), total ion currents to the HFS (c) and LFS (d) plates, and divertor leg integrated D_α brightness across the HFS (e) and LFS legs (f) as function of line-averaged upstream density. The data were taken in JET-ILW in horizontal (black) and vertical (red) divertor plasma configurations shown in the insert.

Fig. 9: Radial profiles of the assumed radial particle (a) and thermal diffusivities (b), and comparison of the measured (symbols) to simulated (lines) electron densities (c,e,g) and

temperatures (d,f,h) at the LFS midplane. The same diffusivity profiles are assumed for the three n_{up} cases and JET-C and JET-ILW considered here: $n_{e,sep,LFS\text{-}mp} = 7x10^{18}$ m^{-3} (c,d), $1.2x10^{19}$ m^{-3} (e,f), and $2.1x10^{19}$ m^{-3} (g,h). The JET-C cases are shown in black, the JET-ILW in red. The n_e profiles include data from HRTS, the Li beam, and the RCP, the T_e profile from HRTS and the RCP.

Fig. 10: EDGE2D/EIRENE predictions of the total radiated power (a), in D (b) and in C, Be, W (c), conducted power to the LFS plate (c), total ion current to the LFS plate (d), and T_e at the LFS plate separatrix (e) as function of upstream electron density at the separatrix. The black curves refer to the C case, the red to the ILW one. The open symbols connected by dashed lines show the predictions based on a linearised EIRENE model, the closed symbols connected by solid lines a more complete EIRENE model, including molecular ions.

Fig. 11: Comparison of the measured (symbols) and predicted (lines) total radiated power in the SOL (a,b), total radiated power in the divertor (c,d), conducted power to the LFS plate (e,f), total ion currents to the LFS plates (g,h), peak electron temperature (i,j), and D_α emission integrated over the LFS leg (k,l) for JET-C wall (left column) and JET-ILW (right column) L-mode plasmas in horizontal configuration. The data is plotted as a function of upstream electron density at the separatrix. The simulated curves in black and right indicate the lower and upper bounds of the assumed power across the grid core boundary.

Fig. 12: Predicted ion currents to the LFS plate (a) and electron temperature at the LFS plate separatrix (b) as a function of electron density at the LFS midplane separatrix. The black curves represent the horizontal and the red curves a corresponding vertical configuration.

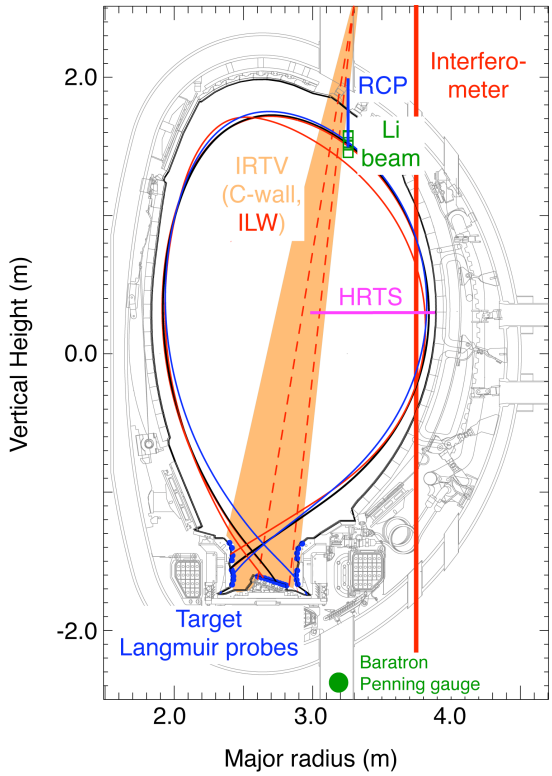
Interfero-
meter
RCP
Li
beam
IRTV
(C-wall,
ILW)
HRTS
Target
Langmuir probes
Baratron
Penning gauge
2.0
0.0
-2.0
Vertical Height (m)
2.0
3.0
4.0
Major radius (m)

Fig. 1

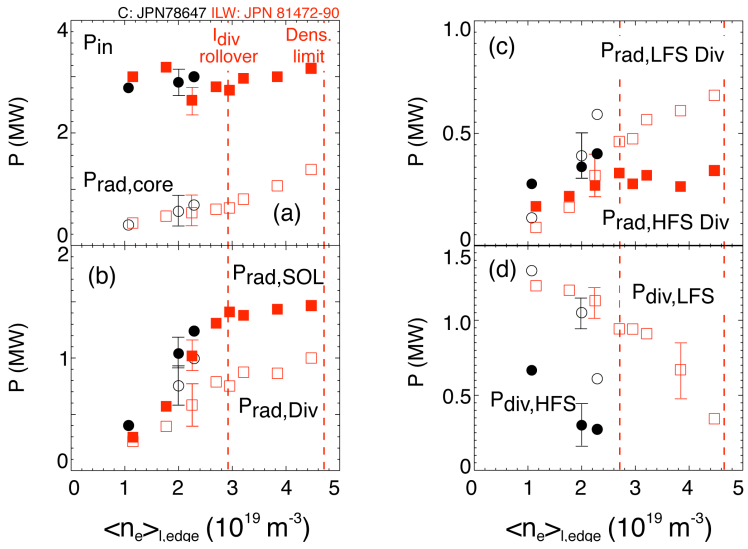
C: JPN78647 ILW: JPN 81472-90
P_in
I_div rollover
Dens. limit
P_rad,core
(a)
(b)
P_rad,SOL
P_rad,Div
(c)
P_rad,LFS Div
P_rad,HFS Div
(d)
P_div,LFS
P_div,HFS
P (MW)
<n_e>_l.edge (10^19 m^-3)

Fig. 2

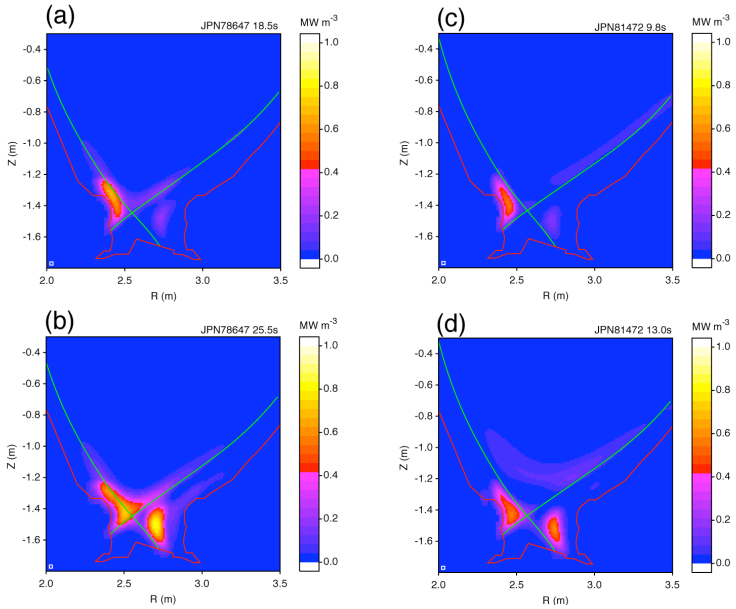
(a)
JPN78647 18.5s
(b)
JPN78647 25.5s
(c)
JPN81472 9.8s
(d)
JPN81472 13.0s
MW m-3
Z (m)
R (m)

Fig. 3

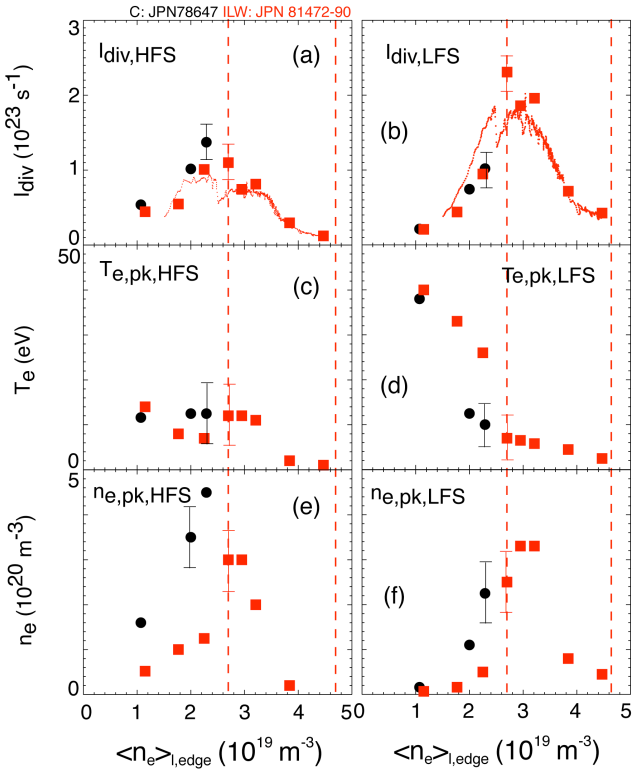
C: JPN78647 ILW: JPN 81472-90
Idiv,HFS
(a)
Idiv,LFS
(b)
Idiv (10^23 s^-1)
Te,pk,HFS
(c)
Te,pk,LFS
(d)
Te (eV)
ne,pk,HFS
(e)
ne,pk,LFS
(f)
ne (10^20 m^-3)
<ne>l,edge (10^19 m^-3)
<ne>l,edge (10^19 m^-3)

Fig. 4

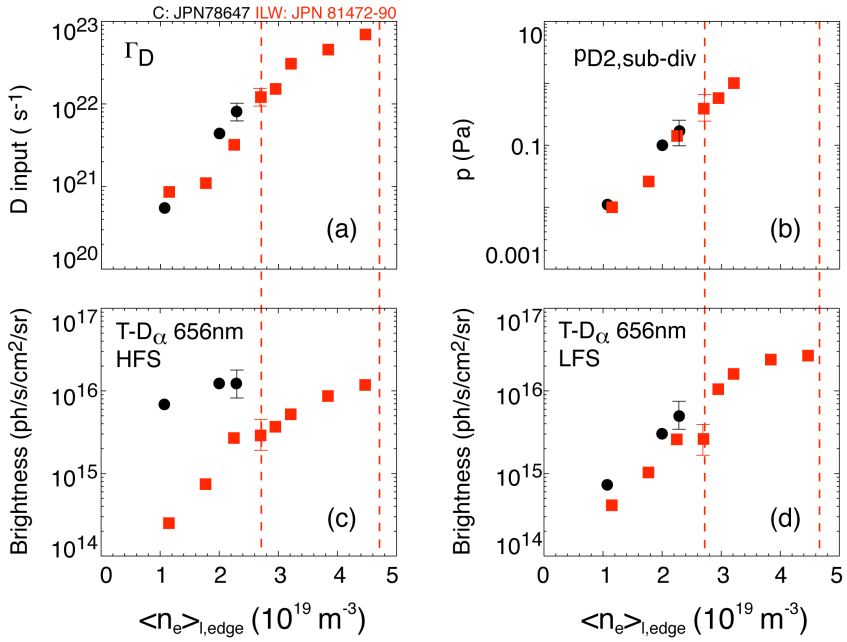
C: JPN78647 ILW: JPN 81472-90
Γ_D
D input (s^{-1})
(a)
pD2,sub-div
p (Pa)
(b)
T-D$_\alpha$ 656nm
HFS
Brightness (ph/s/cm^2/sr)
(c)
T-D$_\alpha$ 656nm
LFS
(d)
<n_e>$_{l,edge}$ (10^{19} m^{-3})

Fig. 5

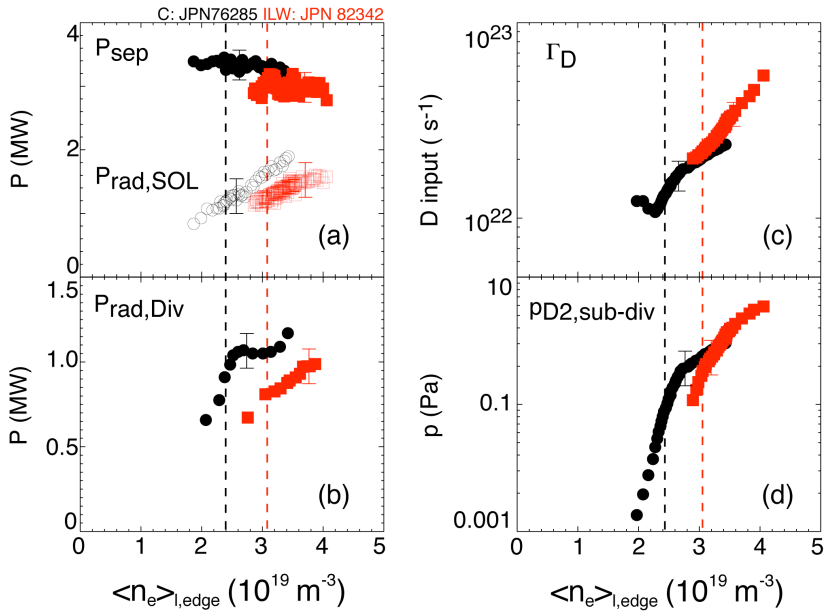
C: JPN76285 ILW: JPN 82342
P (MW)
Psep
Prad,SOL
(a)
Prad,Div
(b)
<ne>l,edge (10^19 m^-3)
D input (s^-1)
ΓD
(c)
pD2,sub-div
p (Pa)
(d)
<ne>l,edge (10^19 m^-3)

Fig. 6

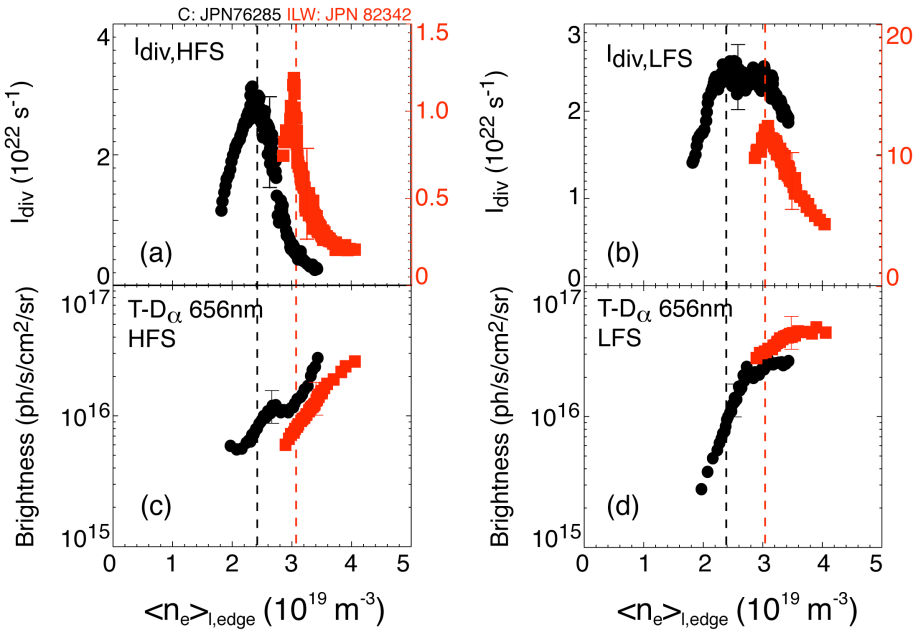
C: JPN76285 ILW: JPN 82342
I_div,HFS
I_div,LFS
(a)
(b)
(c)
(d)
T-Dα 656nm HFS
T-Dα 656nm LFS
I_div (10^22 s^-1)
Brightness (ph/s/cm^2/sr)
<n_e>_l,edge (10^19 m^-3)

Fig. 7

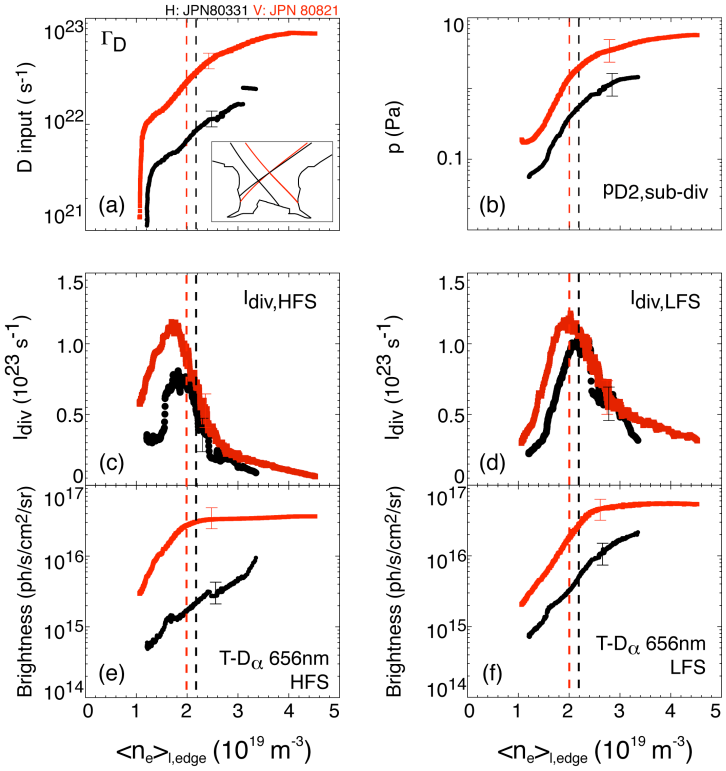
H: JPN80331 V: JPN 80821
Γ_D
D input (s^{-1})
(a)
p (Pa)
pD2,sub-div
(b)
$I_{div,HFS}$
I_{div} (10^{23} s^{-1})
(c)
$I_{div,LFS}$
(d)
Brightness (ph/s/cm^2/sr)
(e)
T-D$_\alpha$ 656nm HFS
(f)
T-D$_\alpha$ 656nm LFS
<n_e>$_{l,edge}$ (10^{19} m^{-3})

Fig. 8

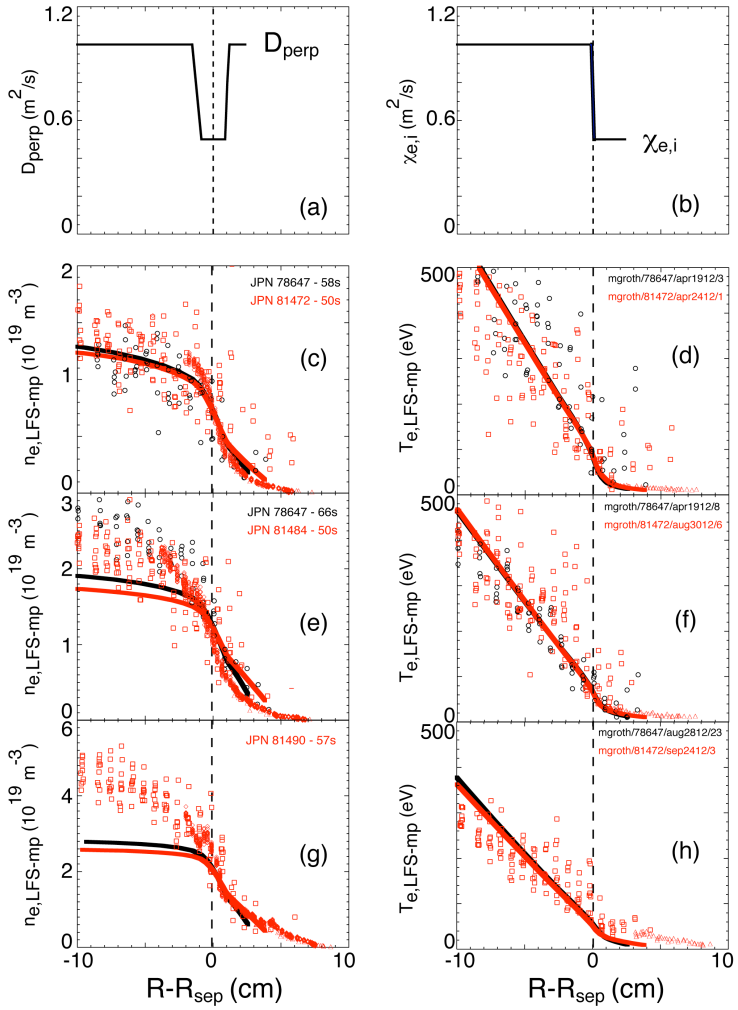
D_perp (m^2/s)
D_perp
(a)
χ_e,i (m^2/s)
χ_e,i
(b)
n_e,LFS-mp (10^19 m^-3)
JPN 78647 - 58s
JPN 81472 - 50s
(c)
T_e,LFS-mp (eV)
mgroth/78647/apr1912/3
mgroth/81472/apr2412/1
(d)
JPN 78647 - 66s
JPN 81484 - 50s
(e)
mgroth/78647/apr1912/8
mgroth/81472/aug3012/6
(f)
JPN 81490 - 57s
(g)
mgroth/78647/aug2812/23
mgroth/81472/sep2412/3
(h)
R-R_sep (cm)

Fig. 9

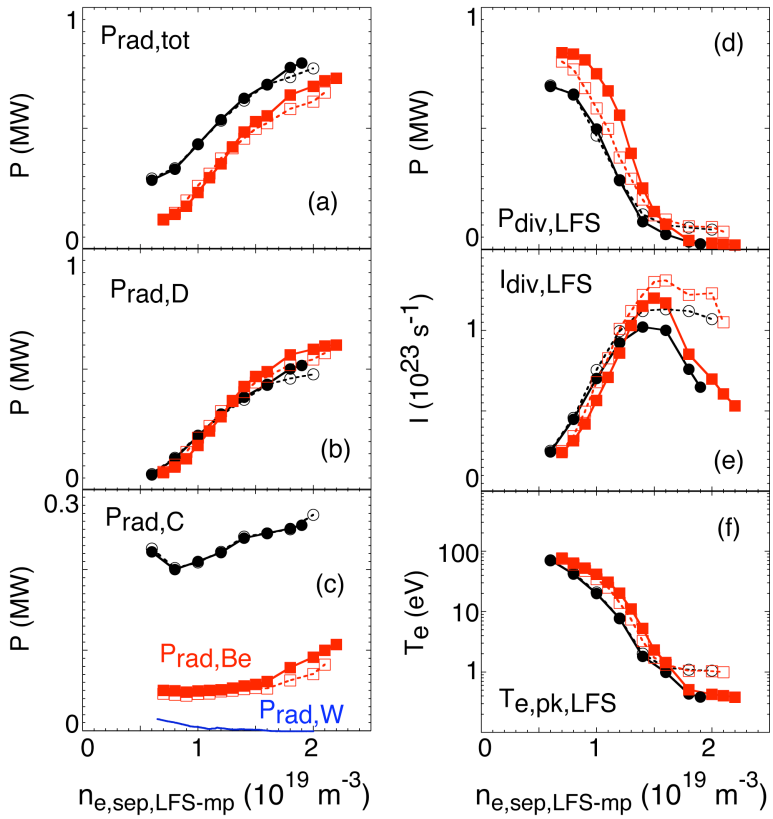
Prad,tot
(a)
Prad,D
(b)
Prad,C
(c)
Prad,Be
Prad,W
P (MW)
(d)
Pdiv,LFS
Idiv,LFS
(e)
I (10^23 s^-1)
(f)
Te,pk,LFS
Te (eV)
ne,sep,LFS-mp (10^19 m^-3)

Fig. 10

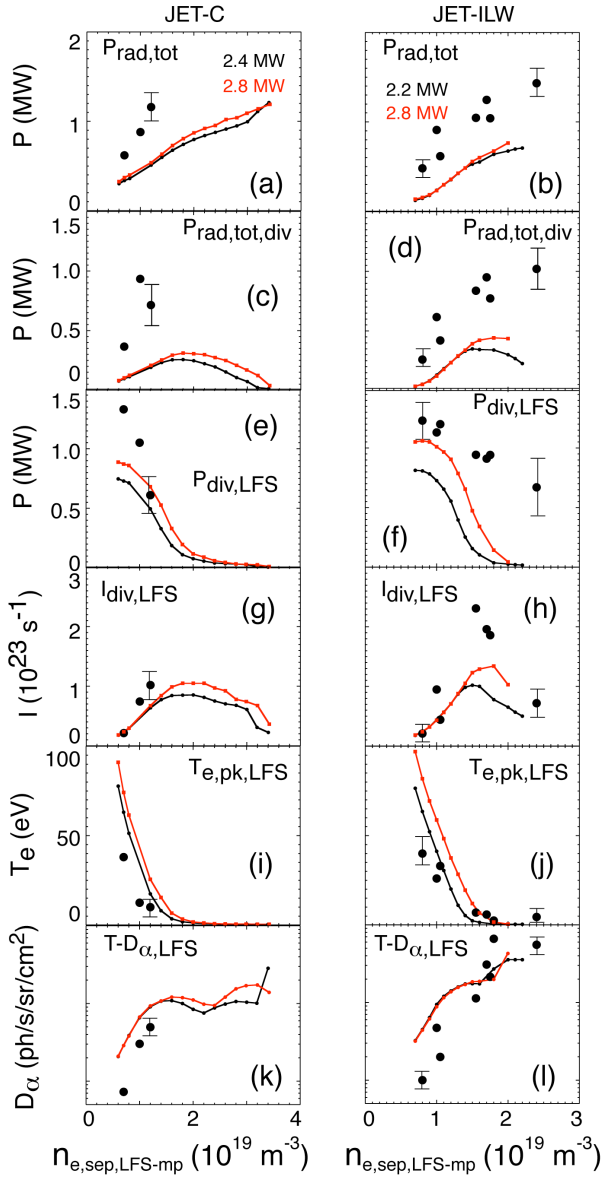
JET-C
JET-ILW
P (MW)
I (10^23 s^-1)
Te (eV)
Dα (ph/s/sr/cm^2)
Prad,tot
2.4 MW
2.8 MW
2.2 MW
2.8 MW
(a)
(b)
Prad,tot,div
(c)
(d)
Pdiv,LFS
(e)
(f)
Idiv,LFS
(g)
(h)
Te,pk,LFS
(i)
(j)
T-Dα,LFS
(k)
(l)
ne,sep,LFS-mp (10^19 m^-3)
ne,sep,LFS-mp (10^19 m^-3)

Fig. 11

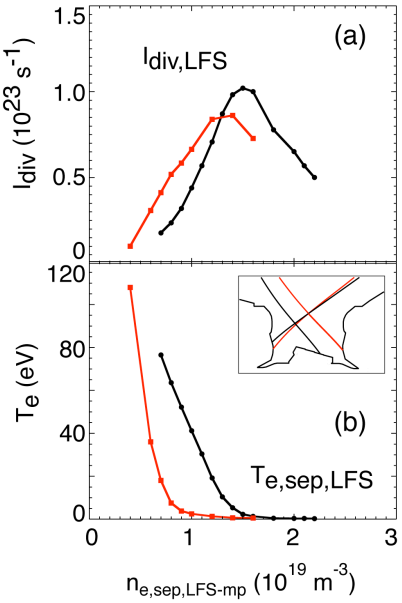
(a)
$I_{div,LFS}$
I_{div} (10^{23} s^{-1})
1.5
1.0
0.5
0
(b)
$T_{e,sep,LFS}$
T_e (eV)
120
80
40
0
0
1
2
3
$n_{e,sep,LFS-mp}$ (10^{19} m^{-3})

Fig. 12